

On Calibrating Diffusion Probabilistic Models

Tianyu Pang¹ Cheng Lu² Chao Du¹ Min Lin¹ Shuicheng Yan¹ Zhijie Deng³

Abstract

Recently, diffusion probabilistic models (DPMs) have achieved promising results in diverse generative tasks. A typical DPM framework includes a forward process that gradually diffuses the data distribution and a reverse process that recovers the data distribution from time-dependent data scores. In this work, we observe that the stochastic reverse process of data scores is a martingale, from which concentration bounds and the optional stopping theorem for data scores can be derived. Then, we discover a simple way for *calibrating* an arbitrary pretrained DPM, with which the score matching loss can be reduced and the lower bounds of model likelihood can consequently be increased. We provide general calibration guidelines under various model parametrizations. Our calibration method is performed only once and the resulting models can be used repeatedly for sampling. We conduct experiments on multiple datasets to empirically validate our proposal. Our code is at <https://github.com/thudzj/Calibrated-DPMs>.

1. Introduction

In the past few years, denoising diffusion probabilistic modeling (Sohl-Dickstein et al., 2015; Ho et al., 2020) and score-based Langevin dynamics (Song & Ermon, 2019; 2020) have demonstrated appealing results on generating images. Later, Song et al. (2021c) unify these two generative learning mechanisms through stochastic/ordinary differential equations. In the following we refer to this unified model family as diffusion probabilistic models (DPMs).

The emerging success of DPMs has attracted broad interest in downstream applications, including image generation (Dhariwal & Nichol, 2021; Vahdat et al., 2021; Karras et al., 2022), shape generation (Cai et al., 2020), video generation (Ho et al., 2022a;b), super-resolution (Saharia et al., 2022), speech synthesis (Chen et al., 2021), graph gener-

ation (Xu et al., 2022), textual inversion (Gal et al., 2022; Ruiz et al., 2022), and text-to-image large models (Rombach et al., 2022; Ramesh et al., 2022), just to name a few.

A typical framework of DPMs involves a *forward* process gradually diffusing the data distribution $q_0(x_0)$ towards a noise distribution $q_T(x_T)$. The transition probability for $t \in [0, T]$ is a conditional Gaussian distribution $q_{0t}(x_t|x_0) = \mathcal{N}(x_t|\alpha_t x_0, \sigma_t^2 \mathbf{I})$, where $\alpha_t, \sigma_t \in \mathbb{R}^+$. Song et al. (2021c) show that there exist *reverse* SDE/ODE processes starting from $q_T(x_T)$ and sharing the same marginal distributions $q_t(x_t)$ as the forward process. The only unknown term in the reverse processes is the data score $\nabla_{x_t} \log q_t(x_t)$, which can be approximated by a time-dependent score model $s_\theta^t(x_t)$ (or with other model parametrizations). $s_\theta^t(x_t)$ is typically learned via score matching (SM) (Hyvärinen, 2005).

In this work, we observe that the stochastic process of the scaled data score $\alpha_t \nabla_{x_t} \log q_t(x_t)$ is a *martingale* w.r.t. the reverse-time process of x_t from T to 0, where the timestep t can be either continuous or discrete. Along the reverse-time sampling path, this martingale property leads to concentration bounds for scaled data scores. Moreover, a martingale satisfies the optional stopping theorem that the expected value at a stopping time is equal to its initial expected value.

Based on the martingale property of data scores, for any $t \in [0, T]$ and any pretrained score model $s_\theta^t(x_t)$ (or with other model parametrizations), we can *calibrate* the model by subtracting its expectation over $q_t(x_t)$, i.e., $\mathbb{E}_{q_t(x_t)} [s_\theta^t(x_t)]$. We formally demonstrate that the calibrated score model $s_\theta^t(x_t) - \mathbb{E}_{q_t(x_t)} [s_\theta^t(x_t)]$ achieves lower values of SM objectives. By the connections between SM objectives and model likelihood of the SDE process (Song et al., 2021b; Kingma et al., 2021) or the ODE process (Lu et al., 2022a), the calibrated score model has higher evidence lower bounds. Similar conclusions also hold for the conditional case, in which we calibrate a conditional score model $s_\theta^t(x_t, y)$ by subtracting its conditional expectation $\mathbb{E}_{q_t(x_t|y)} [s_\theta^t(x_t, y)]$.

In practice, $\mathbb{E}_{q_t(x_t)} [s_\theta^t(x_t)]$ or $\mathbb{E}_{q_t(x_t|y)} [s_\theta^t(x_t, y)]$ can be approximated using noisy training data when the score model has been pretrained. We can also utilize an auxiliary shallow model to estimate these expectations dynamically during pretraining. When we do not have access to training data, we could calculate the expectations using data generated from $s_\theta^t(x_t)$ or $s_\theta^t(x_t, y)$. In experiments, we evaluate

¹Sea AI Lab. ²Department of Computer Science, Tsinghua University. ³Qing Yuan Research Institute, Shanghai Jiao Tong University. Correspondence to: Tianyu Pang <tianyupang@sea.com>, Zhijie Deng <zhijied@sjtu.edu.cn>.

our calibration tricks on the CIFAR-10 (Krizhevsky & Hinton, 2009) and CelebA 64×64 (Liu et al., 2015) datasets, reporting the FID scores (Heusel et al., 2017). We also provide insightful visualization results on the AFHQv2 (Choi et al., 2020), FFHQ (Karras et al., 2019) and ImageNet (Deng et al., 2009) at 64×64 resolution.

2. Diffusion Probabilistic Models

In this section, we briefly review the notations and training paradigms used in diffusion probabilistic models (DPMs). While recent works develop DPMs based on general corruptions (Bansal et al., 2022; Daras et al., 2022), we mainly focus on conventional Gaussian-based DPMs.

2.1. Forward Process

We consider a k -dimensional random variable $x \in \mathbb{R}^k$ and define a *forward* diffusion process on x as $\{x_t\}_{t \in [0, T]}$ with $T > 0$, which satisfies $\forall t \in [0, T]$,

$$x_0 \sim q_0(x_0), \quad q_{0t}(x_t|x_0) = \mathcal{N}(x_t|\alpha_t x_0, \sigma_t^2 \mathbf{I}). \quad (1)$$

Here $q_0(x_0)$ is the data distribution; α_t and σ_t are two positive real-valued functions that are differentiable w.r.t. t with bounded derivatives. Let $q_t(x_t) = \int q_{0t}(x_t|x_0)q_0(x_0)dx_0$ be the marginal distribution of x_t . The schedules of α_t, σ_t^2 need to ensure that $q_T(x_T) \approx \mathcal{N}(x_T|0, \tilde{\sigma}^2 \mathbf{I})$ for some $\tilde{\sigma}$. Kingma et al. (2021) prove that there exists a stochastic differential equation (SDE) satisfying the forward transition distribution in Eq. (1), and this SDE can be written as

$$dx_t = f(t)x_t dt + g(t)d\omega_t, \quad (2)$$

where $\omega_t \in \mathbb{R}^k$ is the standard Wiener process, $f(t)$ and $g(t)$ satisfy $f(t) = \frac{d \log \alpha_t}{dt}$ and $g(t)^2 = \frac{d \sigma_t^2}{dt} - 2 \frac{d \log \alpha_t}{dt} \sigma_t^2$.

2.2. Reverse Process

Song et al. (2021c) demonstrate that the forward SDE in Eq. (2) corresponds to a *reverse* SDE constructed as

$$dx_t = [f(t)x_t - g(t)^2 \nabla_{x_t} \log q_t(x_t)] dt + g(t)d\bar{\omega}_t, \quad (3)$$

where $\bar{\omega}_t \in \mathbb{R}^k$ is the standard Wiener process in reverse time. Starting from $q_T(x_T)$, the marginal distribution of the reverse SDE process is also $q_t(x_t)$ for $t \in [0, T]$. There also exists a deterministic process described by an ordinary differential equation (ODE) as

$$\frac{dx_t}{dt} = f(t)x_t - \frac{1}{2}g(t)^2 \nabla_{x_t} \log q_t(x_t), \quad (4)$$

which starts from $q_T(x_T)$ and shares the same marginal distribution $q_t(x_t)$ as the reverse SDE in Eq. (3). Moreover, by Tweedie’s formula (Efron, 2011), we know that

$$\alpha_t \mathbb{E}_{q_{0t}(x_0|x_t)}[x_0] = x_t + \sigma_t^2 \nabla_{x_t} \log q_t(x_t), \quad (5)$$

where $q_{0t}(x_0|x_t) = \frac{q_{0t}(x_t|x_0)q_0(x_0)}{q_t(x_t)}$.

2.3. Training Paradigm of DPMs

To estimate the data score $\nabla_{x_t} \log q_t(x_t)$ at timestep t , a score-based model $s_\theta^t(x_t)$ (Song et al., 2021c) with shared parameters θ is trained to minimize the score matching (SM) objective (Hyvärinen, 2005) as

$$\mathcal{J}_{\text{SM}}^t(\theta) \triangleq \frac{1}{2} \mathbb{E}_{q_t(x_t)} [\|s_\theta^t(x_t) - \nabla_{x_t} \log q_t(x_t)\|_2^2]. \quad (6)$$

To eliminate the intractable computation of $\nabla_{x_t} \log q_t(x_t)$, denoising score matching (DSM) (Vincent, 2011) transforms $\mathcal{J}_{\text{SM}}^t(\theta)$ into

$$\mathcal{J}_{\text{DSM}}^t(\theta) \triangleq \frac{1}{2} \mathbb{E}_{q_0(x_0), q(\epsilon)} \left[\left\| s_\theta^t(x_t) + \frac{\epsilon}{\sigma_t} \right\|_2^2 \right], \quad (7)$$

where $x_t = \alpha_t x_0 + \sigma_t \epsilon$ and $q(\epsilon) = \mathcal{N}(\epsilon|0, \mathbf{I})$ is a standard Gaussian distribution. Under mild boundary conditions, we know $\mathcal{J}_{\text{SM}}^t(\theta)$ and $\mathcal{J}_{\text{DSM}}^t(\theta)$ is equivalent up to a constant, i.e., $\mathcal{J}_{\text{SM}}^t(\theta) = \mathcal{J}_{\text{DSM}}^t(\theta) + C^t$ and C^t is a constant independent of the model parameters θ . Other SM variants (Song et al., 2019; Pang et al., 2020) are also applicable here.

The total SM objective for training is a weighted sum of $\mathcal{J}_{\text{SM}}^t(\theta)$ across $t \in [0, T]$, defined as

$$\mathcal{J}_{\text{SM}}(\theta; \lambda(t)) \triangleq \int_0^T \lambda(t) \mathcal{J}_{\text{SM}}^t(\theta) dt, \quad (8)$$

where $\lambda(t)$ is a positive weighting function. Similarly, the total DSM objective is $\mathcal{J}_{\text{DSM}}(\theta; \lambda(t)) \triangleq \int_0^T \lambda(t) \mathcal{J}_{\text{DSM}}^t(\theta) dt$. The cases using other model parametrizations such as noise prediction $\epsilon_\theta^t(x_t)$ (Ho et al., 2020; Rombach et al., 2022), data prediction $x_\theta^t(x_t)$ (Kingma et al., 2021; Ramesh et al., 2022), and velocity prediction $v_\theta^t(x_t)$ (Salimans & Ho, 2022; Ho et al., 2022a) are recapped in Appendix B.1.

2.4. Likelihood of DPMs

Suppose that the reverse processes start from a tractable prior $p_T(x_T) = \mathcal{N}(x_T|0, \tilde{\sigma}^2 \mathbf{I})$. We can approximate the reverse-time SDE process by substituting $\nabla_{x_t} \log q_t(x_t)$ with $s_\theta^t(x_t)$ in Eq. (3) as

$$dx_t = [f(t)x_t - g(t)^2 s_\theta^t(x_t)] dt + g(t)d\bar{\omega}_t, \quad (9)$$

which induces the marginal distribution $p_t^{\text{SDE}}(x_t; \theta)$ for any $t \in [0, T]$. In particular, at timestep $t = 0$, the KL divergence between $q_0(x_0)$ and $p_0^{\text{SDE}}(x_0; \theta)$ can be bounded by the total SM objective $\mathcal{J}_{\text{SM}}(\theta; g(t)^2)$ with the weighing function of $g(t)^2$, as stated below:

Lemma 1. (Proof in Song et al. (2021b)) *Let $q_t(x_t)$ be constructed from the forward process in Eq. (2). Then under some regularity conditions, we have*

$$\mathcal{D}_{\text{KL}}(q_0 \| p_0^{\text{SDE}}(\theta)) \leq \mathcal{J}_{\text{SM}}(\theta; g(t)^2) + \mathcal{D}_{\text{KL}}(q_T \| p_T).$$

Here $\mathcal{D}_{\text{KL}}(q_T \| p_T)$ is the prior loss that is independent of θ . Similarly, we approximate the reverse-time ODE process by substituting $\nabla_{x_t} \log q_t(x_t)$ with $\mathbf{s}_\theta^t(x_t)$ in Eq. (4) as

$$\frac{dx_t}{dt} = f(t)x_t - \frac{1}{2}g(t)^2 \mathbf{s}_\theta^t(x_t), \quad (10)$$

which induces the marginal distribution $p_t^{\text{ODE}}(x_t; \theta)$ for any $t \in [0, T]$. By the instantaneous change of variables formula (Chen et al., 2018), change in $\log p_t^{\text{ODE}}(x_t; \theta)$ follows

$$\frac{\log p_t^{\text{ODE}}(x_t; \theta)}{dt} = -\text{tr} \left(\nabla_{x_t} \left(f(t)x_t - \frac{1}{2}g(t)^2 \mathbf{s}_\theta^t(x_t) \right) \right),$$

where $\text{tr}(\cdot)$ denotes the trace of a matrix. Integrating change in $\log p_t^{\text{ODE}}(x_t; \theta)$ from $t = 0$ to T can give the value of $\log p_T(x_T) - \log p_0^{\text{ODE}}(x_0; \theta)$, but requires tracking the path from x_0 to x_T . On the other hand, Lu et al. (2022a) propose that at timestep $t = 0$, the KL divergence between $q_0(x_0)$ and $p_0^{\text{ODE}}(x_0; \theta)$ can be decomposed as stated below:

Lemma 2. (Proof in Lu et al. (2022a)) Let $q_t(x_t)$ be constructed from the forward process in Eq. (2). Then under some regularity conditions, we have

$$\mathcal{D}_{\text{KL}}(q_0 \| p_0^{\text{ODE}}(\theta)) = \mathcal{J}_{\text{SM}}(\theta; g(t)^2) + \mathcal{D}_{\text{KL}}(q_T \| p_T) + \mathcal{J}_{\text{Diff}}(\theta),$$

where the term $\mathcal{J}_{\text{Diff}}(\theta)$ measures the difference between $\mathbf{s}_\theta^t(x_t)$ and $\nabla_{x_t} \log p_t^{\text{ODE}}(x_t; \theta)$ as

$$\mathcal{J}_{\text{Diff}}(\theta) \triangleq \frac{1}{2} \int_0^T g(t)^2 \mathbb{E}_{q_t(x_t)} \left[\left(\mathbf{s}_\theta^t(x_t) - \nabla_{x_t} \log q_t(x_t) \right)^\top \left(\nabla_{x_t} \log p_t^{\text{ODE}}(x_t; \theta) - \mathbf{s}_\theta^t(x_t) \right) \right].$$

Directly computing $\mathcal{J}_{\text{Diff}}(\theta)$ is intractable due to the term $\nabla_{x_t} \log p_t^{\text{ODE}}(x_t; \theta)$. However, we could bound $\mathcal{J}_{\text{Diff}}(\theta)$ via bounding high-order SM objectives.

3. Calibrating Pretrained DPMs

In this section we begin with deriving the relationship between data scores at different timesteps, which leads us to a straightforward method for calibrating any pretrained DPMs. We further analyze the effects of calibration on model likelihood and provide instantiations under conditional cases.

3.1. The Stochastic Process of Data Score

According to Kingma et al. (2021), the form of the forward process in Eq. (1) can be generalized to any two timesteps $0 \leq s < t \leq T$. Then, the transition probability from x_s to x_t is written as

$$q_{st}(x_t | x_s) = \mathcal{N} \left(x_t \middle| \alpha_{t|s} x_s, \sigma_{t|s}^2 \mathbf{I} \right), \quad (11)$$

where $\alpha_{t|s} = \frac{\alpha_t}{\alpha_s}$ and $\sigma_{t|s}^2 = \sigma_t^2 - \alpha_{t|s}^2 \sigma_s^2$. Here the marginal distribution satisfies $q_t(x_t) = \int q_{st}(x_t | x_s) q_s(x_s) dx_s$. We can generally derive the connection between data scores $\nabla_{x_t} \log q_t(x_t)$ and $\nabla_{x_s} \log q_s(x_s)$ as stated below:

Theorem 1. (Proof in Appendix A.1) Let $q_t(x_t)$ be constructed from the forward process in Eq. (2). Then under some regularity conditions, we have $\forall 0 \leq s < t \leq T$,

$$\alpha_t \nabla_{x_t} \log q_t(x_t) = \mathbb{E}_{q_{st}(x_s | x_t)} [\alpha_s \nabla_{x_s} \log q_s(x_s)], \quad (12)$$

where $q_{st}(x_s | x_t) = \frac{q_{st}(x_t | x_s) q_s(x_s)}{q_t(x_t)}$.

Theorem 1 indicates that the stochastic process of $\alpha_t \nabla_{x_t} \log q_t(x_t)$ is a *martingale* w.r.t. the reverse-time process of x_t from timestep T to 0. From the optional stopping theorem (Grimmett & Stirzaker, 2001), the expected value of a martingale at a stopping time is equal to its initial expected value $\mathbb{E}_{q_0(x_0)} [\nabla_{x_0} \log q_0(x_0)]$. Thus, a straightforward corollary (under a mild boundary condition as detailed in Appendix A.2) derived from Theorem 1 is that

$$\mathbb{E}_{q_t(x_t)} [\nabla_{x_t} \log q_t(x_t)] = 0, \quad (13)$$

which holds for $\forall t \in [0, T]$. Besides, the martingale property of the (scaled) data score $\alpha_t \nabla_{x_t} \log q_t(x_t)$ leads to concentration bounds using Azuma’s inequality and Doob’s martingale inequality as derived in Appendix A.3.

3.2. A Simple Calibration Trick

Given a pretrained model $\mathbf{s}_\theta^t(x_t)$ in practice, there is usually $\mathbb{E}_{q_t(x_t)} [\mathbf{s}_\theta^t(x_t)] \neq 0$, despite the fact that the expect data score is zero as indicated in Eq. (13). This motivates us to calibrate $\mathbf{s}_\theta^t(x_t)$ to $\mathbf{s}_\theta^t(x_t) - \eta_t$, where η_t is a time-dependent calibration term that is independent of any particular input x_t . The calibrated SM objective is written as follows:

$$\begin{aligned} \mathcal{J}_{\text{SM}}^t(\theta, \eta_t) &\triangleq \frac{1}{2} \mathbb{E}_{q_t(x_t)} [\|\mathbf{s}_\theta^t(x_t) - \eta_t - \nabla_{x_t} \log q_t(x_t)\|_2^2] \\ &= \mathcal{J}_{\text{SM}}^t(\theta) - \mathbb{E}_{q_t(x_t)} [\mathbf{s}_\theta^t(x_t)]^\top \eta_t + \frac{1}{2} \|\eta_t\|_2^2, \end{aligned} \quad (14)$$

where the second equation holds after the results of $\mathbb{E}_{q_t(x_t)} [\nabla_{x_t} \log q_t(x_t)] = 0$, and there is $\mathcal{J}_{\text{SM}}^t(\theta, 0) = \mathcal{J}_{\text{SM}}^t(\theta)$ specifically when $\eta_t = 0$. Note that the orange part in Eq. (14) is a quadratic function w.r.t. η_t . We look for the optimal $\eta_t^* = \arg \min_{\eta_t} \mathcal{J}_{\text{SM}}^t(\theta, \eta_t)$ that minimizes the calibrated SM objective, from which we can derive

$$\eta_t^* = \mathbb{E}_{q_t(x_t)} [\mathbf{s}_\theta^t(x_t)]. \quad (15)$$

After taking η_t^* into $\mathcal{J}_{\text{SM}}^t(\theta, \eta_t)$, we have

$$\mathcal{J}_{\text{SM}}^t(\theta, \eta_t^*) = \mathcal{J}_{\text{SM}}^t(\theta) - \frac{1}{2} \|\mathbb{E}_{q_t(x_t)} [\mathbf{s}_\theta^t(x_t)]\|_2^2. \quad (16)$$

For other variants of the SM objective, e.g., the DSM objective, since there is $\mathcal{J}_{\text{SM}}^t(\theta) = \mathcal{J}_{\text{DSM}}^t(\theta) + C^t$, we have

$$\mathcal{J}_{\text{DSM}}^t(\theta, \eta_t^*) = \mathcal{J}_{\text{DSM}}^t(\theta) - \frac{1}{2} \|\mathbb{E}_{q_t(x_t)} [\mathbf{s}_\theta^t(x_t)]\|_2^2. \quad (17)$$

It can be easily demonstrated that similar calibration tricks are also valid under other model parametrizations and SM variants, as formally described in Appendix B.2.

Remark. The conclusions in Eq. (16) and Eq. (17) indicate that for any pretrained score model $s_\theta^t(x_t)$, we can calibrate it into $s_\theta^t(x_t) - \mathbb{E}_{q_t(x_t)}[s_\theta^t(x_t)]$, which reduces the SM/DSM objectives at timestep t by $\frac{1}{2} \|\mathbb{E}_{q_t(x_t)}[s_\theta^t(x_t)]\|_2^2$. The expectation of the calibrated score model is always zero, i.e., $\mathbb{E}_{q_t(x_t)}[s_\theta^t(x_t) - \mathbb{E}_{q_t(x_t)}[s_\theta^t(x_t)]] = 0$ holds for any θ , which is consistent with Eq. (13) satisfied by data scores.

3.3. Calibrating Conditional DPMs

In the case of conditional DPMs, we usually employ a conditional model $s_\theta^t(x_t, y)$, where $y \in \mathcal{Y}$ is the conditional context (e.g., class label or text prompt). To learn the conditional data score $\nabla_{x_t} \log q_t(x_t|y) = \nabla_{x_t} \log q_t(x_t, y)$, we minimize the SM objective defined as

$$\mathcal{J}_{\text{SM}}^t(\theta) \triangleq \frac{1}{2} \mathbb{E}_{q_t(x_t, y)} [\|s_\theta^t(x_t, y) - \nabla_{x_t} \log q_t(x_t, y)\|_2^2].$$

Similar to Eq. (13), there is $\mathbb{E}_{q_t(x_t|y)}[\nabla_{x_t} \log q_t(x_t|y)] = 0$. To calibrate $s_\theta^t(x_t, y)$, we use the conditional term $\eta_t(y)$ and the calibrated SM objective is formulated as

$$\begin{aligned} \mathcal{J}_{\text{SM}}^t(\theta, \eta_t(y)) &\triangleq \frac{1}{2} \mathbb{E}_{q_t(x_t, y)} [\|s_\theta^t(x_t, y) - \eta_t(y) - \nabla_{x_t} \log q_t(x_t, y)\|_2^2] \\ &= \mathcal{J}_{\text{SM}}^t(\theta) - \mathbb{E}_{q_t(x_t, y)} \left[s_\theta^t(x_t, y)^\top \eta_t(y) + \frac{1}{2} \|\eta_t(y)\|_2^2 \right], \end{aligned}$$

and for any $y \in \mathcal{Y}$, the optimal $\eta_t^*(y)$ is given by

$$\eta_t^*(y) = \mathbb{E}_{q_t(x_t|y)}[s_\theta^t(x_t, y)].$$

After taking $\eta_t^*(y)$ into $\mathcal{J}_{\text{SM}}^t(\theta, \eta_t(y))$, we have

$$\mathcal{J}_{\text{SM}}^t(\theta, \eta_t^*(y)) = \mathcal{J}_{\text{SM}}^t(\theta) - \frac{1}{2} \mathbb{E}_{q_t(y)} [\|\mathbb{E}_{q_t(x_t|y)}[s_\theta^t(x_t, y)]\|_2^2].$$

This calibration form can naturally generalize to other model parametrizations and SM variants in conditional cases.

4. Properties of Calibrated DPMs

In this section, we investigate the properties of calibrated DPMs, including their model likelihood, conservative preserving, and calibration term computation.

4.1. Likelihood of Calibrated DPMs

Now we discuss the effects of calibration on model likelihood. Following the notations in Section 2.4, we use $p_0^{\text{SDE}}(\theta, \eta_t)$ and $p_0^{\text{ODE}}(\theta, \eta_t)$ to denote the distributions induced by the reverse-time SDE and ODE processes, respectively, where $\nabla_{x_t} \log q_t(x_t)$ is substituted with $s_\theta^t(x_t) - \eta_t$.

Likelihood of $p_0^{\text{SDE}}(\theta, \eta_t)$. According to Lemma 1, we have

$$\mathcal{D}_{\text{KL}}(q_0 \| p_0^{\text{SDE}}(\theta, \eta_t)) \leq \mathcal{J}_{\text{SM}}(\theta, \eta_t; g(t)^2) + \mathcal{D}_{\text{KL}}(q_T \| p_T),$$

where $\mathcal{J}_{\text{SM}}(\theta, \eta_t; g(t)^2) \triangleq \int_0^T g(t)^2 \mathcal{J}_{\text{SM}}^t(\theta, \eta_t) dt$ is the total SM objective after the score model is calibrated by η_t . From the result in Eq. (16), there is

$$\begin{aligned} \mathcal{J}_{\text{SM}}(\theta, \eta_t^*; g(t)^2) &= \mathcal{J}_{\text{SM}}(\theta; g(t)^2) - \frac{1}{2} \int_0^T g(t)^2 \|\mathbb{E}_{q_t(x_t)}[s_\theta^t(x_t)]\|_2^2 dt. \end{aligned} \quad (18)$$

Therefore, the likelihood $\mathcal{D}_{\text{KL}}(q_0 \| p_0^{\text{SDE}}(\theta, \eta_t^*))$ after calibration has a lower upper bound of $\mathcal{J}_{\text{SM}}(\theta, \eta_t^*; g(t)^2) + \mathcal{D}_{\text{KL}}(q_T \| p_T)$, compared to the bound of $\mathcal{J}_{\text{SM}}(\theta; g(t)^2) + \mathcal{D}_{\text{KL}}(q_T \| p_T)$ for the original $\mathcal{D}_{\text{KL}}(q_0 \| p_0^{\text{SDE}}(\theta))$.¹

Likelihood of $p_0^{\text{ODE}}(\theta, \eta_t)$. Note that in Lemma 2, there is a term $\mathcal{J}_{\text{Diff}}(\theta)$, which is usually small in practice since $s_\theta^t(x_t)$ and $\nabla_{x_t} \log p_t^{\text{ODE}}(x_t; \theta)$ are close. Thus, we have

$$\mathcal{D}_{\text{KL}}(q_0 \| p_0^{\text{ODE}}(\theta, \eta_t)) \approx \mathcal{J}_{\text{SM}}(\theta, \eta_t; g(t)^2) + \mathcal{D}_{\text{KL}}(q_T \| p_T),$$

and $\mathcal{D}_{\text{KL}}(q_0 \| p_0^{\text{ODE}}(\theta, \eta_t^*))$ approximately achieves its lowest value. Lu et al. (2022a) show that $\mathcal{D}_{\text{KL}}(q_0 \| p_0^{\text{ODE}}(\theta))$ can be further bounded by high-order SM objectives (as detailed in Appendix A.4), which depend on $\nabla_{x_t} s_\theta^t(x_t)$ and $\nabla_{x_t} \text{tr}(\nabla_{x_t} s_\theta^t(x_t))$. Since the calibration term η_t is independent of x_t , i.e., $\nabla_{x_t} \eta_t = 0$, it does not affect the values of high-order SM objectives, and achieves a lower upper bound due to the lower value of the first-order SM objective.

4.2. Conservative Preserving

A theoretical flaw of score-based modeling is that $s_\theta^t(x_t)$ may not correspond to a probability distribution. To solve this issue, Salimans & Ho (2021) develop an energy-based model design, which utilizes the power of score-based modeling and simultaneously makes sure that $s_\theta^t(x_t)$ is conservative, i.e., there exists a probability distribution $p_\theta^t(x_t)$ such that $\forall x_t \in \mathbb{R}^k$, we have $s_\theta^t(x_t) = \nabla_{x_t} \log p_\theta^t(x_t)$. In this case, after we calibrate $s_\theta^t(x_t)$ by subtracting η_t , there is

$$s_\theta^t(x_t) - \eta_t = \nabla_{x_t} \log \left(\frac{p_\theta^t(x_t)}{\exp(x_t^\top \eta_t) Z_t(\theta)} \right), \quad (19)$$

where $Z_t(\theta) = \int p_\theta^t(x_t) \exp(-x_t^\top \eta_t) dx_t$ represents the normalization factor. Intuitively, subtracting by η_t corresponds to a shift in the vector space, so if $s_\theta^t(x_t)$ is conservative, its calibrated version $s_\theta^t(x_t) - \eta_t$ is also conservative.

4.3. Amortized Computation of $\mathbb{E}_{q_t(x_t)}[s_\theta^t(x_t)]$

By default, we are able to calculate and restore the value of $\mathbb{E}_{q_t(x_t)}[s_\theta^t(x_t)]$ for a pretrained model $s_\theta^t(x_t)$, where

¹Note that $\mathcal{D}_{\text{KL}}(q_0 \| p_0^{\text{SDE}}(\theta, \eta_t^*))$ is not necessarily smaller than $\mathcal{D}_{\text{KL}}(q_0 \| p_0^{\text{SDE}}(\theta))$ since we can only compare their upper bounds.

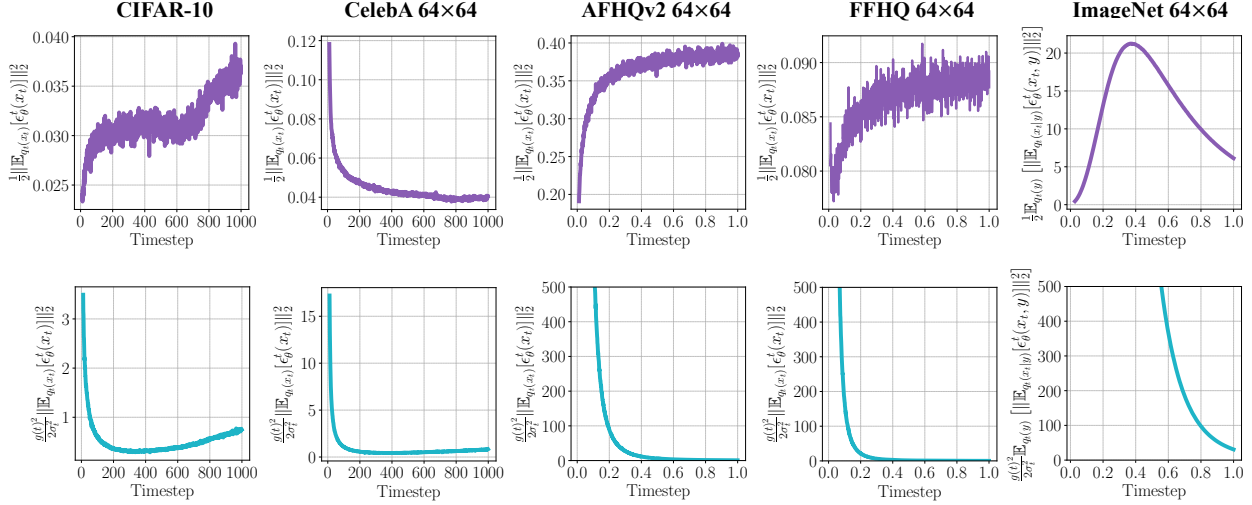


Figure 1. The time-dependent values of $\frac{1}{2} \|\mathbb{E}_{q_t(x_t)} [\epsilon_\theta^t(x_t)]\|_2^2$ (the first row) and $\frac{g(t)^2}{2\sigma_t^2} \|\mathbb{E}_{q_t(x_t)} [\epsilon_\theta^t(x_t)]\|_2^2$ (the second row) calculated on different datasets. The models on CIFAR-10 and CelebA is trained on discrete timesteps ($t = 0, 1, \dots, 1000$), while those on AFHQv2, FFHQ, and ImageNet are trained on continuous timesteps ($t \in [0, 1]$). We convert data prediction $\hat{x}_\theta^t(x_t)$ into noise prediction $\epsilon_\theta^t(x_t)$ based on $\epsilon_\theta^t(x_t) = (x_t - \alpha_t \hat{x}_\theta^t(x_t))/\sigma_t$. The y-axis is clamped into $[0, 500]$.

the selection of timestep t is determined by the inference algorithm, and the expectation over $q_t(x_t)$ can be approximated by Monte Carlo sampling from a noisy training set. When we do not have access to training data, we can approximate the expectation using data generated from $p_t^{\text{ODE}}(x_t; \theta)$ or $p_t^{\text{SDE}}(x_t; \theta)$. Since we only need to calculate $\mathbb{E}_{q_t(x_t)} [s_\theta^t(x_t)]$ once, the raised computational overhead is amortized as the number of generated samples increases.

Dynamically recording. In the preceding context, we focus primarily on post-training computing of $\mathbb{E}_{q_t(x_t)} [s_\theta^t(x_t)]$. An alternative strategy would be to dynamically record $\mathbb{E}_{q_t(x_t)} [s_\theta^t(x_t)]$ during the pretraining phase of $s_\theta^t(x_t)$. Specifically, we could construct an auxiliary shallow network $h_\phi(t)$ parameterized by ϕ , whose input is the timestep t . We define the expected mean squared error as

$$\mathcal{J}_{\text{Cal}}^t(\phi) \triangleq \mathbb{E}_{q_t(x_t)} [\|h_\phi(t) - s_\theta^t(x_t)^\dagger\|_2^2], \quad (20)$$

where the superscript \dagger denotes the stopping gradient and ϕ^* is the optimal solution of minimizing $\mathcal{J}_{\text{Cal}}^t(\phi)$ w.r.t. ϕ , satisfying $h_{\phi^*}(t) = \eta_t^* = \mathbb{E}_{q_t(x_t)} [s_\theta^t(x_t)]$ (assuming sufficient model capacity). The total training objective can therefore be expressed as $\mathcal{J}_{\text{SM}}(\theta; \lambda(t)) + \int_0^T \beta_t \cdot \mathcal{J}_{\text{Cal}}^t(\phi)$, where β_t is a time-dependent trade-off coefficient for $t \in [0, T]$.

5. Experiments

In this section, we demonstrate that sample quality and model likelihood can be both improved by calibrating DPMs. Instead of establishing a new state-of-the-art, the purpose of our empirical studies is to testify the efficacy of our calibration technique as a simple way to repair DPMs.

5.1. Sample Quality

While training-time calibration is feasible, we primarily focus on calibrating publicly available pretrained DPMs.

Setup. We apply post-training calibration to discrete-time models trained on CIFAR-10 (Krizhevsky & Hinton, 2009) and CelebA (Liu et al., 2015), which apply *parametrization of noise prediction* $\epsilon_\theta^t(x_t)$. In the sampling phase, we employ DPM-Solver (Lu et al., 2022b), an ODE-based sampler that achieves a promising balance between sample efficiency and image quality. In accordance with the recommendation,² we set the end time of DPM-Solver to 10^{-3} when the number of sampling steps is less than 15, and to 10^{-4} otherwise. Additional details can be found in Lu et al. (2022b). By default, we employ the FID score (Heusel et al., 2017) to quantify the sample quality using 50,000 samples. Typically, a lower FID indicates a higher sample quality.

Computing $\mathbb{E}_{q_t(x_t)} [\epsilon_\theta^t(x_t)]$. To estimate the expectation over $q_t(x_t)$, we construct $x_t = \alpha_t x_0 + \sigma_t \epsilon$, where $x_0 \sim q_0(x_0)$ is sampled from the training set and $\epsilon \sim \mathcal{N}(\epsilon | \mathbf{0}, \mathbf{I})$ is sampled from a standard Gaussian distribution. The selection of timestep t depends on the sampling schedule of DPM-Solver. The computed values of $\mathbb{E}_{q_t(x_t)} [\epsilon_\theta^t(x_t)]$ are restored in a dictionary and warped into the output layers of DPMs, allowing existing inference pipelines to be reused.

We first calibrate the model trained by Ho et al. (2020) on the CIFAR-10 dataset and compare it to the original one for sampling with DPM-Solvers. We conduct a systematic study with varying NFE (i.e., number of function

²<https://github.com/LuChengTHU/dpm-solver>

Table 1. Comparison on sample quality measured by FID \downarrow with varying NFE on the CIFAR-10 dataset. Experiments are conducted using a linear noise schedule on the discrete-time model from Ho et al. (2020). We consider three variants of DPM-Solver with different orders. The results with \dagger mean the actual NFE is order $\times \lfloor \frac{\text{NFE}}{\text{order}} \rfloor$ which is smaller than the given NFE, following the setting in Lu et al. (2022b).

Noise prediction	DPM-Solver	Number of evaluations (NFE)						
		10	15	20	25	30	35	40
$\epsilon_\theta^t(x_t)$	1-order	20.49	12.47	9.72	7.89	6.84	6.22	5.75
	2-order	7.35	\dagger 4.52	4.14	\dagger 3.92	3.74	\dagger 3.71	3.68
	3-order	\dagger 23.96	4.61	\dagger 3.89	\dagger 3.73	3.65	\dagger 3.65	\dagger 3.60
$\epsilon_\theta^t(x_t) - \mathbb{E}_{q_t(x_t)}[\epsilon_\theta^t(x_t)]$	1-order	19.31	11.77	8.86	7.35	6.28	5.76	5.36
	2-order	6.76	\dagger 4.36	4.03	\dagger 3.66	3.54	\dagger 3.44	3.48
	3-order	\dagger 53.50	4.22	\dagger 3.32	\dagger 3.33	3.35	\dagger 3.32	\dagger 3.31

Table 2. Comparison on sample quality measured by FID \downarrow with varying NFE on CelebA 64 \times 64. Experiments are conducted using a linear noise schedule on the discrete-time model from (Song et al., 2021a). The settings of DPM-Solver are the same as on CIFAR-10.

Noise prediction	DPM-Solver	Number of evaluations (NFE)						
		10	15	20	25	30	35	40
$\epsilon_\theta^t(x_t)$	1-order	16.74	11.85	7.93	6.67	5.90	5.38	5.01
	2-order	4.32	\dagger 3.98	2.94	\dagger 2.88	2.88	\dagger 2.88	2.84
	3-order	\dagger 11.92	3.91	\dagger 2.84	\dagger 2.76	2.82	\dagger 2.81	\dagger 2.85
$\epsilon_\theta^t(x_t) - \mathbb{E}_{q_t(x_t)}[\epsilon_\theta^t(x_t)]$	1-order	16.13	11.29	7.09	6.06	5.28	4.87	4.39
	2-order	4.42	\dagger 3.94	2.61	\dagger 2.66	2.54	\dagger 2.52	2.49
	3-order	\dagger 35.47	3.62	\dagger 2.33	\dagger 2.43	2.40	\dagger 2.43	\dagger 2.49

evaluations) and solver order. The results are presented in Table 1. After calibrating the model, the sample quality is consistently enhanced, which demonstrates the significance of doing so and the efficacy of our method. We highlight the significant improvement in sample quality (4.61 \rightarrow 4.22 when using 15 NFE and 3-order DPM-Solver; 3.89 \rightarrow 3.32 when using 20 NFE and 3-order DPM-Solver). After model calibration, the number of steps required to achieve convergence for a 3-order DPM-Solver is reduced from ≥ 30 to 20. Specifically, our method represents a potential new option for expediting the sampling of DPMs. In addition, as a point of comparison, the 3-order DPM-Solver with 1,000 NFE can only yield an FID score of 3.45 when using the original model, which, along with the results in Table 1, indicates that model calibration likely helps to improve the convergence of sampling. We also note that a higher-order DPM-Solver is superior to a lower-order one, regardless of whether the model has been calibrated.

Then, we conduct experiments with the discrete-time model trained on the CelebA 64 \times 64 dataset by Song et al. (2021a). The corresponding sample quality comparison is shown in Table 2. Clearly, model calibration brings significant gains (3.91 \rightarrow 3.62 when using 15 NFE and 3-order DPM-Solver; 2.84 \rightarrow 2.33 when using 20 NFE and 3-order DPM-Solver) that are consistent with those on the CIFAR-10 dataset. This demonstrates the prevalence of the mis-calibration issue in existing DPMs and the efficacy of our correction. We still

observe that model calibration improves convergence of sampling. Generated images are visualized in Appendix C.

5.2. Model Likelihood

As described in Section 4.1, calibration contributes to reducing the SM objective, thereby decreasing the upper bound of the KL divergence between model distribution at timestep $t = 0$ (either $p_0^{\text{SDE}}(\theta, \eta_t^*)$ or $p_0^{\text{ODE}}(\theta, \eta_t^*)$) and data distribution q_0 . Consequently, it aids in raising the lower bound of model likelihood. In this subsection, we examine such effects by evaluating the aforementioned DPMs on the CIFAR-10 and CelebA datasets. We also conduct experiments with continuous-time models trained by Karras et al. (2022) on AFHQv2 64 \times 64 (Choi et al., 2020), FFHQ 64 \times 64 (Karras et al., 2019), and ImageNet 64 \times 64 (Deng et al., 2009) datasets considering their top performance.³ These models apply parametrization of data prediction $\mathbf{x}_\theta^t(x_t)$, and for consistency, we convert it to align with $\epsilon_\theta^t(x_t)$ based on the relationship $\epsilon_\theta^t(x_t) = (x_t - \alpha_t \mathbf{x}_\theta^t(x_t))/\sigma_t$, as detailed in Kingma et al. (2021) and Appendix B.2.

Given that we are employing noise prediction models in practice, we first estimate $\frac{1}{2} \|\mathbb{E}_{q_t(x_t)}[\epsilon_\theta^t(x_t)]\|_2^2$ at timestep $t \in [0, T]$, which reflects the decrement on the SM objective at t according to Eq. (16) (up to a scaling factor of $1/\sigma_t^2$). We approximate the expectation using Monte

³We use pretrained models in <https://github.com/NVlabs/edm>

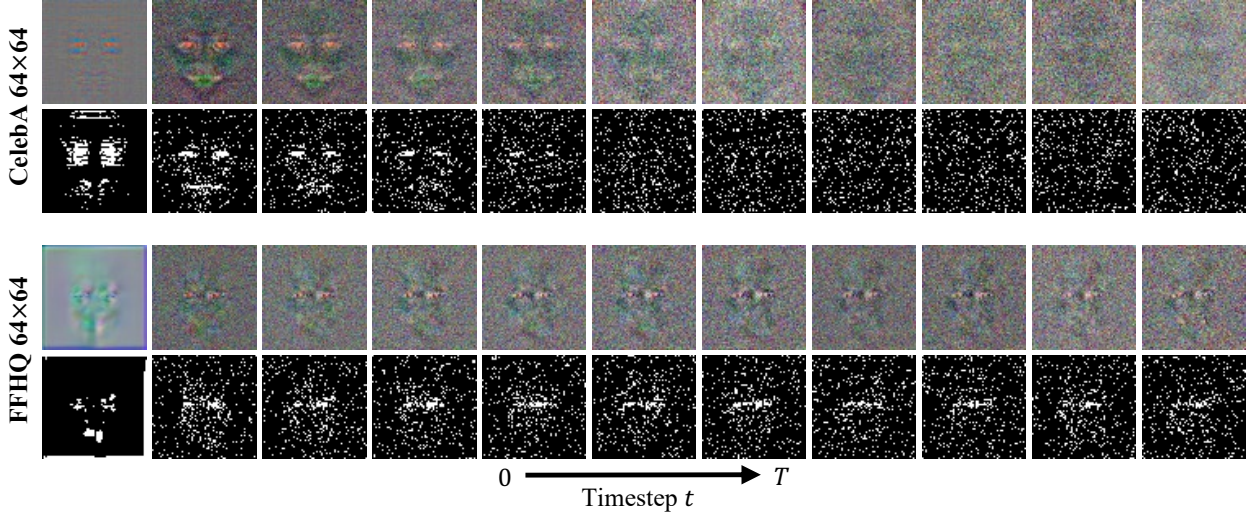


Figure 2. Visualization of the expected predicted noises with increasing t . For each dataset, the first row displays $\mathbb{E}_{q_t(x_t)} [\epsilon_\theta^t(x_t)]$ (after normalization) and the second row highlights the top-10% pixels that $\mathbb{E}_{q_t(x_t)} [\epsilon_\theta^t(x_t)]$ has high values. The DPM on CelebA is a discrete-time model with 1000 timesteps (Song et al., 2021a) and that on FFHQ is a continuous-time one (Karras et al., 2022).

Carlo (MC) estimation with training data points. The results are displayed in the first row of Figure 1. Notably, the value of $\frac{1}{2} \|\mathbb{E}_{q_t(x_t)} [\epsilon_\theta^t(x_t)]\|_2^2$ varies significantly along with timestep t : it decreases relative to t for CelebA but increases relative to t in all other cases (except for $t \in [0.4, 1.0]$ on ImageNet 64×64). Theoretically, according to Eq. (13), there should be $\frac{1}{2} \|\mathbb{E}_{q_t(x_t)} [\nabla_{x_t} \log q_t(x_t)]\|_2^2 = 0$ at any t . Such inconsistency reveals that mis-calibration issues exist in general, although the details of the phenomenon may vary across datasets and training mechanisms.

Then, we quantify the gain of model calibration on increasing the lower bound of model likelihood, which is mathematically $\frac{1}{2} \int_0^T g(t)^2 \|\mathbb{E}_{q_t(x_t)} [s_\theta^t(x_t)]\|_2^2 dt$ according to Eq. (18). We first rewrite it with the model parametrization of noise prediction $\epsilon_\theta^t(x_t)$, and it can be straightforwardly demonstrated that it equals $\int_0^T \frac{g(t)^2}{2\sigma_t^2} \|\mathbb{E}_{q_t(x_t)} [\epsilon_\theta^t(x_t)]\|_2^2$. Therefore, we calculate the value of $\frac{g(t)^2}{2\sigma_t^2} \|\mathbb{E}_{q_t(x_t)} [\epsilon_\theta^t(x_t)]\|_2^2$ using MC estimation and report the results in the second row of Figure 1. The integral is represented by the area under the curve (i.e., the gain of model calibration on the lower bound of model likelihood).

Various datasets and model architectures exhibit nontrivial gains, as observed. In addition, we notice that the DPMs trained by Karras et al. (2022) show patterns distinct from those of DDPM (Ho et al., 2020) and DDIM (Song et al., 2021a), from which we conclude that different DPM training mechanisms may result in different mis-calibration effects. So we advocate taking the calibration issue into account when designing new techniques for training DPMs.

Visualizing $\mathbb{E}_{q_t(x_t)} [\epsilon_\theta^t(x_t)]$. To better understand the inductive bias learned by DPMs, we visualize the expected predicted noises $\mathbb{E}_{q_t(x_t)} [\epsilon_\theta^t(x_t)]$ for timestep from 0 to T ,

as seen in Figure 2. For each dataset, the first row normalizes the values of $\mathbb{E}_{q_t(x_t)} [\epsilon_\theta^t(x_t)]$ into $[0, 255]$; the second row calculates pixel-wise norm (across RGB channels) and highlights the top-10% locations with the highest norm. As we can observe, on facial datasets like CelebA and FFHQ, there are obvious facial patterns inside $\mathbb{E}_{q_t(x_t)} [\epsilon_\theta^t(x_t)]$, while on other datasets like CIFAR-10, ImageNet, as well as the animal face dataset AFHQv2, the patterns inside $\mathbb{E}_{q_t(x_t)} [\epsilon_\theta^t(x_t)]$ are more like random noises. Besides, the facial patterns in Figure 2 are more significant when t is smaller, and become blurry when t is close to T . This phenomenon may be attributed to the memorization of training data, which is detrimental to generalization during sampling and justifies the importance of calibration.

5.3. Ablation Studies

We conduct ablation studies of the calibration method, focusing on estimation methods of $\mathbb{E}_{q_t(x_t)} [\epsilon_\theta^t(x_t)]$.

Estimating $\mathbb{E}_{q_t(x_t)} [\epsilon_\theta^t(x_t)]$ with partial training data. In the post-training calibration setting, our primary algorithmic change is to subtract the calibration term $\mathbb{E}_{q_t(x_t)} [\epsilon_\theta^t(x_t)]$ from the pretrained DPMs' output. In the aforementioned studies, the expectation in $\mathbb{E}_{q_t(x_t)} [\epsilon_\theta^t(x_t)]$ (or its variant of other model parametrizations) is approximated with MC estimation using all training images. However, there may be situations where training data are (partially) inaccessible. To evaluate the effectiveness of our method under these cases, we examine the number of training images used to estimate the calibration term on CIFAR-10. To determine the quality of the estimated calibration term, we sample from the calibrated models using a 3-order DPM-Solver running for 20 steps and evaluate the corresponding FID score. The results are listed in the left part of Table 3. As

Table 3. Sample quality varies w.r.t. the number of training images (left part) and generated images (right part) employed to estimate the calibration term on the CIFAR-10 dataset. In the generated data case, the images used to estimate the calibration term $\mathbb{E}_{q_t(x_t)} [\epsilon_\theta^t(x_t)]$ is crafted with 50 sampling steps by a 3-order DPM-Solver. In both cases, the images used to compute FID scores are crafted with 20 sampling steps by a 3-order DPM-Solver.

Training data		Generated data	
# of samples	FID ↓	# of samples	FID ↓
500	55.38	2,000	8.80
1,000	18.72	5,000	4.53
2,000	8.05	10,000	3.78
5,000	4.31	20,000	3.31
10,000	3.47	50,000	3.46
20,000	3.25	100,000	3.47
50,000	3.32	200,000	3.46

observed, we need to use the majority of training images (at least $\geq 20,000$) to estimate the calibration term. We deduce that this is because the CIFAR-10 images are rich in diversity, necessitating a non-trivial number of training images to cover the various modes and produce a nearly unbiased calibration term.

Estimating $\mathbb{E}_{q_t(x_t)} [\epsilon_\theta^t(x_t)]$ with generated data. In the most extreme case where we do not have access to any training data (e.g., due to privacy concerns), we could still estimate the expectation over $q_t(x_t)$ with data generated from $p_0^{\text{ODE}}(x_0; \theta)$ or $p_0^{\text{SDE}}(x_0; \theta)$. Specifically, under the hypothesis that $p_0^{\text{ODE}}(x_0; \theta) \approx q_0(x_0)$ (DPM-Solver is an ODE-based sampler), we first generate $\tilde{x}_0 \sim p_0^{\text{ODE}}(x_0; \theta)$ and construct $\tilde{x}_t = \alpha_t \tilde{x}_0 + \sigma_t \epsilon$, where $\tilde{x}_t \sim p_t^{\text{ODE}}(x_t; \theta)$. Then, the expectation over $q_t(x_t)$ could be approximated by the expectation over $p_t^{\text{ODE}}(x_t; \theta)$.

Empirically, on the CIFAR-10 dataset, we adopt a 3-order DPM-Solver to generate a set of samples from the pretrained model of Ho et al. (2020), using a relatively large number of sampling steps (e.g., 50 steps). This set of generated data is used to calculate the calibration term $\mathbb{E}_{q_t(x_t)} [\epsilon_\theta^t(x_t)]$. Then, we obtain the calibrated model $\epsilon_\theta^t(x_t) - \mathbb{E}_{q_t(x_t)} [\epsilon_\theta^t(x_t)]$ and craft new images based on a 3-order 20-step DPM-Solver. In the right part of Table 3, we present the results of an empirical investigation into how the number of generated images influences the quality of model calibration.

Using the same sampling setting, we also provide two reference points: 1) the originally mis-calibrated model can reach the FID score of 3.89, and 2) the model calibrated with training data can reach the FID score of 3.32. Comparing these results reveals that the DPM calibrated with a large number of high-quality generations can achieve comparable FID scores to those calibrated with training samples (see the result of using 20,000 generated images). Additionally, it appears that using more generations is not advantageous.

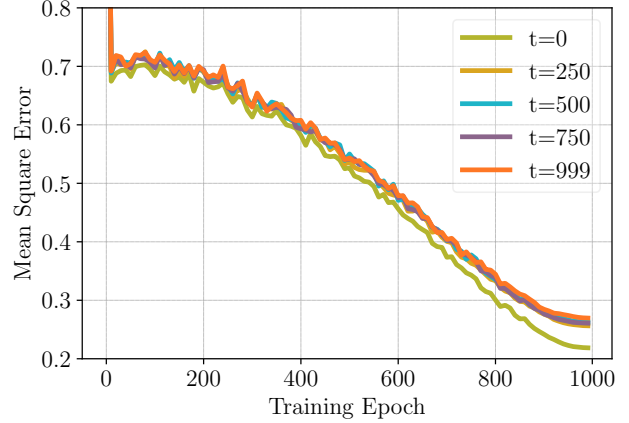


Figure 3. During training, the mean square error between the ground truth and the outputs of a shallow network for recording the calibration terms rapidly decreases.

This may be because the generations from DPMs, despite being known to cover diverse modes, still exhibit semantic redundancy and deviate slightly from the distribution exhibited by the training samples.

Dynamical recording. We simulate the proposed dynamical recording technique. Specifically, we use a 3-layer MLP of width 512 to parameterize the aforementioned network $h_\phi(t)$ and train it with an Adam optimizer (Kingma & Ba, 2014) to approximate the expected predicted noises $\mathbb{E}_{q_t(x_t)} [\epsilon_\theta^t(x_t)]$, where $\epsilon_\theta^t(x_t)$ comes from the pretrained noise prediction model on CIFAR-10 (Ho et al., 2020). The training of $h_\phi(t)$ runs for 1,000 epochs. Meanwhile, using the training data, we compute the expected predicted noises with MC estimation and treat them as the ground truth. In Figure 3, we compare them to the outputs of $h_\phi(t)$ and visualize the disparity measured by mean square error. Due to space constraints, we focus primarily on the outcomes of five representative timesteps. As demonstrated, as the number of training epochs increases, the network $h_\phi(t)$ quickly converges and can form a relatively reliable approximation to the ground truth. Dynamic recording has a distinct advantage of being able to be performed during the training of DPMs to enable immediate generation. We clarify that better timestep embedding techniques and NN architectures can improve approximation quality even further.

6. Conclusion

We propose a simple method for calibrating any pretrained DPM that can provably reduce the values of SM objectives and, as a result, induce higher values of lower bounds for model likelihood. To better understand the inductive bias learned by models, we empirically validate the effectiveness of our calibration trick and visualize the expected predicted noises. Our ablation studies demonstrate the utility of our calibration method and broaden its application range.

References

- Azuma, Kazuoki. Weighted sums of certain dependent random variables. *Tohoku Mathematical Journal, Second Series*, 19(3):357–367, 1967.
- Bansal, Arpit, Borgnia, Eitan, Chu, Hong-Min, Li, Jie S, Kazemi, Hamid, Huang, Furong, Goldblum, Micah, Geiping, Jonas, and Goldstein, Tom. Cold diffusion: Inverting arbitrary image transforms without noise. *arXiv preprint arXiv:2208.09392*, 2022.
- Cai, Ruojin, Yang, Guandao, Averbuch-Elor, Hadar, Hao, Zekun, Belongie, Serge, Snively, Noah, and Hariharan, Bharath. Learning gradient fields for shape generation. In *European Conference on Computer Vision (ECCV)*, 2020.
- Chen, Nanxin, Zhang, Yu, Zen, Heiga, Weiss, Ron J, Norouzi, Mohammad, and Chan, William. Wavegrad: Estimating gradients for waveform generation. In *International Conference on Learning Representations (ICLR)*, 2021.
- Chen, Ricky TQ, Rubanova, Yulia, Bettencourt, Jesse, and Duvenaud, David K. Neural ordinary differential equations. In *Advances in Neural Information Processing Systems (NeurIPS)*, 2018.
- Choi, Yunje, Uh, Youngjung, Yoo, Jaejun, and Ha, Jung-Woo. Stargan v2: Diverse image synthesis for multiple domains. In *IEEE International Conference on Computer Vision (CVPR)*, 2020.
- Daras, Giannis, Delbracio, Mauricio, Talebi, Hossein, Dimakis, Alexandros G, and Milanfar, Peyman. Soft diffusion: Score matching for general corruptions. *arXiv preprint arXiv:2209.05442*, 2022.
- Deng, Jia, Dong, Wei, Socher, Richard, Li, Li-Jia, Li, Kai, and Fei-Fei, Li. Imagenet: A large-scale hierarchical image database. In *IEEE Conference on Computer Vision and Pattern Recognition (CVPR)*, 2009.
- Dhariwal, Prafulla and Nichol, Alexander. Diffusion models beat gans on image synthesis. In *Advances in Neural Information Processing Systems (NeurIPS)*, 2021.
- Doob, Joseph L and Doob, Joseph L. *Stochastic processes*, volume 7. Wiley New York, 1953.
- Efron, Bradley. Tweedie’s formula and selection bias. *Journal of the American Statistical Association*, 106(496): 1602–1614, 2011.
- Gal, Rinon, Alaluf, Yuval, Atzmon, Yuval, Patashnik, Or, Bermano, Amit H, Chechik, Gal, and Cohen-Or, Daniel. An image is worth one word: Personalizing text-to-image generation using textual inversion. *arXiv preprint arXiv:2208.01618*, 2022.
- Grimmett, Geoffrey and Stirzaker, David. *Probability and random processes*. Oxford university press, 2001.
- Heusel, Martin, Ramsauer, Hubert, Unterthiner, Thomas, Nessler, Bernhard, and Hochreiter, Sepp. Gans trained by a two time-scale update rule converge to a local nash equilibrium. In *Advances in Neural Information Processing Systems (NeurIPS)*, pp. 6626–6637, 2017.
- Ho, Jonathan, Jain, Ajay, and Abbeel, Pieter. Denoising diffusion probabilistic models. In *Advances in Neural Information Processing Systems (NeurIPS)*, 2020.
- Ho, Jonathan, Chan, William, Saharia, Chitwan, Whang, Jay, Gao, Ruiqi, Gritsenko, Alexey, Kingma, Diederik P, Poole, Ben, Norouzi, Mohammad, Fleet, David J, et al. Imagen video: High definition video generation with diffusion models. *arXiv preprint arXiv:2210.02303*, 2022a.
- Ho, Jonathan, Salimans, Tim, Gritsenko, Alexey, Chan, William, Norouzi, Mohammad, and Fleet, David J. Video diffusion models. *arXiv preprint arXiv:2204.03458*, 2022b.
- Hyvärinen, Aapo. Estimation of non-normalized statistical models by score matching. *Journal of Machine Learning Research (JMLR)*, 6(Apr):695–709, 2005.
- Karras, Tero, Laine, Samuli, and Aila, Timo. A style-based generator architecture for generative adversarial networks. In *IEEE International Conference on Computer Vision (CVPR)*, 2019.
- Karras, Tero, Aittala, Miika, Aila, Timo, and Laine, Samuli. Elucidating the design space of diffusion-based generative models. In *Advances in Neural Information Processing Systems (NeurIPS)*, 2022.
- Kingma, Diederik, Salimans, Tim, Poole, Ben, and Ho, Jonathan. Variational diffusion models. In *Advances in Neural Information Processing Systems (NeurIPS)*, 2021.
- Kingma, Diederik P and Ba, Jimmy. Adam: A method for stochastic optimization. *arXiv preprint arXiv:1412.6980*, 2014.
- Krizhevsky, Alex and Hinton, Geoffrey. Learning multiple layers of features from tiny images. Technical report, Citeseer, 2009.
- Liu, Ziwei, Luo, Ping, Wang, Xiaogang, and Tang, Xiaoou. Deep learning face attributes in the wild. In *International Conference on Computer Vision (ICCV)*, 2015.
- Lu, Cheng, Zheng, Kaiwen, Bao, Fan, Chen, Jianfei, Li, Chongxuan, and Zhu, Jun. Maximum likelihood training for score-based diffusion odes by high order denoising score matching. In *International Conference on Machine Learning (ICML)*, 2022a.

- Lu, Cheng, Zhou, Yuhao, Bao, Fan, Chen, Jianfei, Li, Chongxuan, and Zhu, Jun. Dpm-solver: A fast ode solver for diffusion probabilistic model sampling in around 10 steps. In *Advances in Neural Information Processing Systems (NeurIPS)*, 2022b.
- Pang, Tianyu, Xu, Kun, Li, Chongxuan, Song, Yang, Ermon, Stefano, and Zhu, Jun. Efficient learning of generative models via finite-difference score matching. In *Advances in Neural Information Processing Systems (NeurIPS)*, 2020.
- Ramesh, Aditya, Dhariwal, Prafulla, Nichol, Alex, Chu, Casey, and Chen, Mark. Hierarchical text-conditional image generation with clip latents. *arXiv preprint arXiv:2204.06125*, 2022.
- Rombach, Robin, Blattmann, Andreas, Lorenz, Dominik, Esser, Patrick, and Ommer, Björn. High-resolution image synthesis with latent diffusion models. In *IEEE Conference on Computer Vision and Pattern Recognition (CVPR)*, 2022.
- Ruiz, Nataniel, Li, Yuanzhen, Jampani, Varun, Pritch, Yael, Rubinstein, Michael, and Aberman, Kfir. Dreambooth: Fine tuning text-to-image diffusion models for subject-driven generation. *arXiv preprint arXiv:2208.12242*, 2022.
- Saharia, Chitwan, Ho, Jonathan, Chan, William, Salimans, Tim, Fleet, David J, and Norouzi, Mohammad. Image super-resolution via iterative refinement. *IEEE Transactions on Pattern Analysis and Machine Intelligence (TPAMI)*, 2022.
- Salimans, Tim and Ho, Jonathan. Should ebms model the energy or the score? In *Energy Based Models Workshop-ICLR*, 2021.
- Salimans, Tim and Ho, Jonathan. Progressive distillation for fast sampling of diffusion models. In *International Conference on Learning Representations (ICLR)*, 2022.
- Sohl-Dickstein, Jascha, Weiss, Eric, Maheswaranathan, Niru, and Ganguli, Surya. Deep unsupervised learning using nonequilibrium thermodynamics. In *International Conference on Machine Learning (ICML)*, pp. 2256–2265. PMLR, 2015.
- Song, Jiaming, Meng, Chenlin, and Ermon, Stefano. Denoising diffusion implicit models. In *International Conference on Learning Representations (ICLR)*, 2021a.
- Song, Yang and Ermon, Stefano. Generative modeling by estimating gradients of the data distribution. In *Advances in Neural Information Processing Systems (NeurIPS)*, pp. 11895–11907, 2019.
- Song, Yang and Ermon, Stefano. Improved techniques for training score-based generative models. In *Advances in Neural Information Processing Systems (NeurIPS)*, 2020.
- Song, Yang, Garg, Sahaj, Shi, Jiaxin, and Ermon, Stefano. Sliced score matching: A scalable approach to density and score estimation. In *Conference on Uncertainty in Artificial Intelligence (UAI)*, 2019.
- Song, Yang, Durkan, Conor, Murray, Iain, and Ermon, Stefano. Maximum likelihood training of score-based diffusion models. In *Advances in Neural Information Processing Systems (NeurIPS)*, 2021b.
- Song, Yang, Sohl-Dickstein, Jascha, Kingma, Diederik P, Kumar, Abhishek, Ermon, Stefano, and Poole, Ben. Score-based generative modeling through stochastic differential equations. In *International Conference on Learning Representations (ICLR)*, 2021c.
- Vahdat, Arash, Kreis, Karsten, and Kautz, Jan. Score-based generative modeling in latent space. In *Advances in Neural Information Processing Systems (NeurIPS)*, 2021.
- Vincent, Pascal. A connection between score matching and denoising autoencoders. *Neural computation*, 23(7): 1661–1674, 2011.
- Xu, Minkai, Yu, Lantao, Song, Yang, Shi, Chence, Ermon, Stefano, and Tang, Jian. Geodiff: A geometric diffusion model for molecular conformation generation. In *International Conference on Learning Representations (ICLR)*, 2022.

A. Detailed Derivations

In this section, we provide detailed derivations for the Theorem and equations shown in the main text. We follow the regularization assumptions listed in [Song et al. \(2021b\)](#).

A.1. Proof of Theorem 1

Proof. For any two timesteps $0 \leq s < t \leq T$, i.e., the transition probability from x_s to x_t is written as $q_{st}(x_t|x_s) = \mathcal{N}(x_t|\alpha_{t|s}x_s, \sigma_{t|s}^2\mathbf{I})$, where $\alpha_{t|s} = \frac{\alpha_t}{\alpha_s}$ and $\sigma_{t|s}^2 = \sigma_t^2 - \alpha_{t|s}^2\sigma_s^2$. The marginal distribution $q_t(x_t) = \int q_{st}(x_t|x_s)q_s(x_s)dx_s$ and we have

$$\begin{aligned}
\nabla_{x_t} \log q_t(x_t) &= \frac{1}{\alpha_{t|s}} \nabla_{\alpha_{t|s}^{-1}x_t} \log \left(\frac{1}{\alpha_{t|s}^k} \mathbb{E}_{\mathcal{N}(x_s|\alpha_{t|s}^{-1}x_t, \alpha_{t|s}^{-2}\sigma_{t|s}^2\mathbf{I})} [q_s(x_s)] \right) \\
&= \frac{1}{\alpha_{t|s}} \nabla_{\alpha_{t|s}^{-1}x_t} \log \left(\mathbb{E}_{\mathcal{N}(\eta|0, \alpha_{t|s}^{-2}\sigma_{t|s}^2\mathbf{I})} [q_s(\alpha_{t|s}^{-1}x_t + \eta)] \right) \\
&= \frac{\mathbb{E}_{\mathcal{N}(\eta|0, \alpha_{t|s}^{-2}\sigma_{t|s}^2\mathbf{I})} [\nabla_{\alpha_{t|s}^{-1}x_t} q_s(\alpha_{t|s}^{-1}x_t + \eta)]}{\alpha_{t|s} \mathbb{E}_{\mathcal{N}(\eta|0, \alpha_{t|s}^{-2}\sigma_{t|s}^2\mathbf{I})} [q_s(\alpha_{t|s}^{-1}x_t + \eta)]} \\
&= \frac{\mathbb{E}_{\mathcal{N}(\eta|0, \alpha_{t|s}^{-2}\sigma_{t|s}^2\mathbf{I})} [q_s(\alpha_{t|s}^{-1}x_t + \eta) \nabla_{\alpha_{t|s}^{-1}x_t + \eta} \log q_s(\alpha_{t|s}^{-1}x_t + \eta)]}{\alpha_{t|s} \mathbb{E}_{\mathcal{N}(\eta|0, \alpha_{t|s}^{-2}\sigma_{t|s}^2\mathbf{I})} [q_s(\alpha_{t|s}^{-1}x_t + \eta)]} \\
&= \frac{\mathbb{E}_{\mathcal{N}(x_s|\alpha_{t|s}^{-1}x_t, \alpha_{t|s}^{-2}\sigma_{t|s}^2\mathbf{I})} [q_s(x_s) \nabla_{x_s} \log q_s(x_s)]}{\alpha_{t|s} \mathbb{E}_{\mathcal{N}(x_s|\alpha_{t|s}^{-1}x_t, \alpha_{t|s}^{-2}\sigma_{t|s}^2\mathbf{I})} [q_s(x_s)]} \\
&= \frac{\int \mathcal{N}(x_t|\alpha_{t|s}x_s, \sigma_{t|s}^2\mathbf{I}) q_s(x_s) \nabla_{x_s} \log q_s(x_s) dx_s}{\alpha_{t|s} \int \mathcal{N}(x_t|\alpha_{t|s}x_s, \sigma_{t|s}^2\mathbf{I}) q_s(x_s) dx_s} \\
&= \frac{1}{\alpha_{t|s}} \mathbb{E}_{q_{st}(x_s|x_t)} [\nabla_{x_s} \log q_s(x_s)].
\end{aligned} \tag{21}$$

Note that when the transition probability $q_{st}(x_t|x_s)$ corresponds to a well-defined forward process, there is $\alpha_t > 0$ for $\forall t \in [0, T]$, and thus we achieve $\alpha_t \nabla_{x_t} \log q_t(x_t) = \mathbb{E}_{q_{st}(x_s|x_t)} [\alpha_s \nabla_{x_s} \log q_s(x_s)]$. \square

A.2. Proof of Eq. (13)

Proof. The input variable $x \in \mathbb{R}^k$ and $q_0(x_0) \in \mathcal{C}^2$, where \mathcal{C}^2 denotes the family of functions with continuous second-order derivatives.⁴ We use x^i denote the i -th element of x , then we can derive the expectation

$$\begin{aligned}
\mathbb{E}_{q_0(x_0)} \left[\frac{\partial}{\partial x_0^i} \log q_0(x_0) \right] &= \int \cdots \int q_0(x_0) \frac{\partial}{\partial x_0^i} \log q_0(x_0) dx_0^1 dx_0^2 \cdots dx_0^k \\
&= \int \cdots \int \frac{\partial}{\partial x_0^i} q_0(x_0) dx_0^1 dx_0^2 \cdots dx_0^k \\
&= \int \frac{\partial}{\partial x_0^i} \left(\int q_0(x_0^i, x_0^{\setminus i}) dx_0^{\setminus i} \right) dx_0^i \\
&= \int \frac{d}{dx_0^i} q_0(x_0^i) dx_0^i = 0,
\end{aligned} \tag{22}$$

where $x_0^{\setminus i}$ denotes all the $k - 1$ elements in x_0 except for the i -th one. The last equation holds under the boundary condition that $\lim_{x_0^i \rightarrow \infty} q_0(x_0^i) = 0$ hold for any $i \in [K]$. Thus, we achieve the conclusion that $\mathbb{E}_{q_0(x_0)} [\nabla_{x_0} \log q_0(x_0)] = 0$. \square

⁴This continuously differentiable assumption can be satisfied by adding a small Gaussian noise (e.g., with variance of 0.0001) on the original data distribution, as done in [Song & Ermon \(2019\)](#).

A.3. Concentration Bounds

We describe concentration bounds (Doob & Doob, 1953; Azuma, 1967) of the martingale $\alpha_t \nabla_{x_t} \log q_t(x_t)$.

Azuma's inequality. For discrete reverse timestep $t = T, T-1, \dots, 0$, Assuming that there exist constants $0 < c_1, c_2, \dots, < \infty$ such that for the i -th element of x ,

$$A_t \leq \frac{\partial}{\partial x_{t-1}^i} \alpha_{t-1} \log q_{t-1}(x_{t-1}) - \frac{\partial}{\partial x_t^i} \alpha_t \log q_t(x_t) \leq B_t \text{ and } B_t - A_t \leq c_t \quad (23)$$

almost surely. Then $\forall \epsilon > 0$, the probability (note that $\alpha_0 = 1$)

$$P \left(\left| \frac{\partial}{\partial x_0^i} \log q_0(x_0) - \frac{\partial}{\partial x_T^i} \alpha_T \log q_T(x_T) \right| \geq \epsilon \right) \leq 2 \exp \left(- \frac{2\epsilon^2}{\sum_{t=1}^T c_t^2} \right). \quad (24)$$

Specially, considering that $q_T(x_T) \approx \mathcal{N}(x_T|0, \tilde{\sigma}^2 \mathbf{I})$, there is $\frac{\partial}{\partial x_T^i} \log q_T(x_T) \approx -\frac{x_T^i}{\tilde{\sigma}^2}$. Thus, we can approximately obtain

$$P \left(\left| \frac{\partial}{\partial x_0^i} \log q_0(x_0) + \frac{\alpha_T x_T^i}{\tilde{\sigma}^2} \right| \geq \epsilon \right) \leq 2 \exp \left(- \frac{2\epsilon^2}{\sum_{t=1}^T c_t^2} \right). \quad (25)$$

Doob's inequality. For continuous reverse timestep t from T to 0 , if the sample paths of the martingale are almost surely right-continuous, then for the i -th element of x we have (note that $\alpha_0 = 1$)

$$P \left(\sup_{0 \leq t \leq T} \frac{\partial}{\partial x_t^i} \alpha_t \log q_t(x_t) \geq C \right) \leq \frac{\mathbb{E}_{q_0(x_0)} \left[\max \left(\frac{\partial}{\partial x_0^i} \log q_0(x_0), 0 \right) \right]}{C}. \quad (26)$$

A.4. High-Order SM Objectives

Lu et al. (2022a) show that the KL divergence $\mathcal{D}_{\text{KL}}(q_0 \| p_0^{\text{ODE}}(\theta))$ can be bounded as

$$\mathcal{D}_{\text{KL}}(q_0 \| p_0^{\text{ODE}}(\theta)) \leq \mathcal{D}_{\text{KL}}(q_T \| p_T) + \sqrt{\mathcal{J}_{\text{SM}}(\theta; g(t)^2)} \cdot \sqrt{\mathcal{J}_{\text{Fisher}}(\theta)}, \quad (27)$$

where $\mathcal{J}_{\text{Fisher}}(\theta)$ is a weighted sum of Fisher divergence between $q_t(x_t)$ and $p_t^{\text{ODE}}(\theta)$ as

$$\mathcal{J}_{\text{Fisher}}(\theta) = \frac{1}{2} \int_0^T g(t)^2 D_F(q_t \| p_t^{\text{ODE}}(\theta)) dt. \quad (28)$$

Moreover, Lu et al. (2022a) prove that if $\forall t \in [0, T]$ and $\forall x_t \in \mathbb{R}^k$, there exist a constant C_F such that the spectral norm of Hessian matrix $\|\nabla_{x_t}^2 \log p_t^{\text{ODE}}(x_t; \theta)\|_2 \leq C_F$, and there exist $\delta_1, \delta_2, \delta_3 > 0$ such that

$$\begin{aligned} \|\mathbf{s}_\theta^t(x_t) - \nabla_{x_t} \log q_t(x_t)\|_2 &\leq \delta_1, \\ \|\nabla_{x_t} \mathbf{s}_\theta^t(x_t) - \nabla_{x_t}^2 \log q_t(x_t)\|_F &\leq \delta_2, \\ \|\nabla_{x_t} \mathbf{tr}(\nabla_{x_t} \mathbf{s}_\theta^t(x_t)) - \nabla_{x_t} \mathbf{tr}(\nabla_{x_t}^2 \log q_t(x_t))\|_2 &\leq \delta_3, \end{aligned} \quad (29)$$

where $\|\cdot\|_F$ is the Frobenius norm of matrix. Then there exist a function $U(t; \delta_1, \delta_2, \delta_3, q)$ that independent of θ and strictly increasing (if $g(t) \neq 0$) w.r.t. δ_1, δ_2 , and δ_3 , respectively, such that the Fisher divergence can be bounded as $D_F(q_t \| p_t^{\text{ODE}}(\theta)) \leq U(t; \delta_1, \delta_2, \delta_3, q)$.

The case after calibration. When we impose the calibration term $\eta_t^* = \mathbb{E}_{q_t(x_t)}[\mathbf{s}_\theta^t(x_t)]$ to get the score model $\mathbf{s}_\theta^t(x_t) - \eta_t^*$, there is $\nabla_{x_t} \eta_t^* = 0$ and thus $\nabla_{x_t}(\mathbf{s}_\theta^t(x_t) - \eta_t^*) = \nabla_{x_t} \mathbf{s}_\theta^t(x_t)$. Then we have

$$\begin{aligned} \|\mathbf{s}_\theta^t(x_t) - \eta_t^* - \nabla_{x_t} \log q_t(x_t)\|_2 &\leq \delta'_1 \leq \delta_1, \\ \|\nabla_{x_t}(\mathbf{s}_\theta^t(x_t) - \eta_t^*) - \nabla_{x_t}^2 \log q_t(x_t)\|_F &\leq \delta_2, \\ \|\nabla_{x_t} \mathbf{tr}(\nabla_{x_t}(\mathbf{s}_\theta^t(x_t) - \eta_t^*)) - \nabla_{x_t} \mathbf{tr}(\nabla_{x_t}^2 \log q_t(x_t))\|_2 &\leq \delta_3. \end{aligned} \quad (30)$$

From these, we know that the Fisher divergence $D_F(q_t \| p_t^{\text{ODE}}(\theta, \eta_t^*)) \leq U(t; \delta'_1, \delta_2, \delta_3, q) \leq U(t; \delta_1, \delta_2, \delta_3, q)$, namely, $D_F(q_t \| p_t^{\text{ODE}}(\theta, \eta_t^*))$ has a lower upper bound compared to $D_F(q_t \| p_t^{\text{ODE}}(\theta))$. Consequently, we can get lower upper bounds for both $\mathcal{J}_{\text{Fisher}}(\theta, \eta_t^*)$ and $\mathcal{D}_{\text{KL}}(q_0 \| p_0^{\text{ODE}}(\theta, \eta_t^*))$, compared to $\mathcal{J}_{\text{Fisher}}(\theta)$ and $\mathcal{D}_{\text{KL}}(q_0 \| p_0^{\text{ODE}}(\theta))$, respectively.

B. Model Parametrization

This section introduces different parametrizations used in diffusion models and provides their calibrated instantiations.

B.1. Preliminary

Along the research routine of diffusion models, different model parametrizations have been used, including score prediction $\mathbf{s}_\theta^t(x_t)$ (Song & Ermon, 2019; Song et al., 2021c), noise prediction $\epsilon_\theta^t(x_t)$ (Ho et al., 2020; Rombach et al., 2022), data prediction $\mathbf{x}_\theta^t(x_t)$ (Kingma et al., 2021; Ramesh et al., 2022), and velocity prediction $\mathbf{v}_\theta^t(x_t)$ (Salimans & Ho, 2022; Ho et al., 2022a). Taking the DSM objective as the training loss, its instantiation at timestep $t \in [0, T]$ is written as

$$\mathcal{J}_{\text{DSM}}^t(\theta) = \begin{cases} \frac{1}{2} \mathbb{E}_{q_0(x_0), q(\epsilon)} \left[\left\| \mathbf{s}_\theta^t(x_t) + \frac{\epsilon}{\sigma_t} \right\|_2^2 \right], & \text{score prediction;} \\ \frac{\alpha_t^2}{2\sigma_t^2} \mathbb{E}_{q_0(x_0), q(\epsilon)} \left[\left\| \mathbf{x}_\theta^t(x_t) - x_0 \right\|_2^2 \right], & \text{data prediction;} \\ \frac{1}{2\sigma_t^2} \mathbb{E}_{q_0(x_0), q(\epsilon)} \left[\left\| \epsilon_\theta^t(x_t) - \epsilon \right\|_2^2 \right], & \text{noise prediction;} \\ \frac{\alpha_t^2}{2\sigma_t^2} \mathbb{E}_{q_0(x_0), q(\epsilon)} \left[\left\| \mathbf{v}_\theta^t(x_t) - (\alpha_t \epsilon - \sigma_t x_0) \right\|_2^2 \right], & \text{velocity prediction.} \end{cases} \quad (31)$$

B.2. Calibrated Instantiation

Under different model parametrizations, we can derive the optimal calibration terms η_t^* that minimizing $\mathcal{J}_{\text{DSM}}^t(\theta, \eta_t)$ as

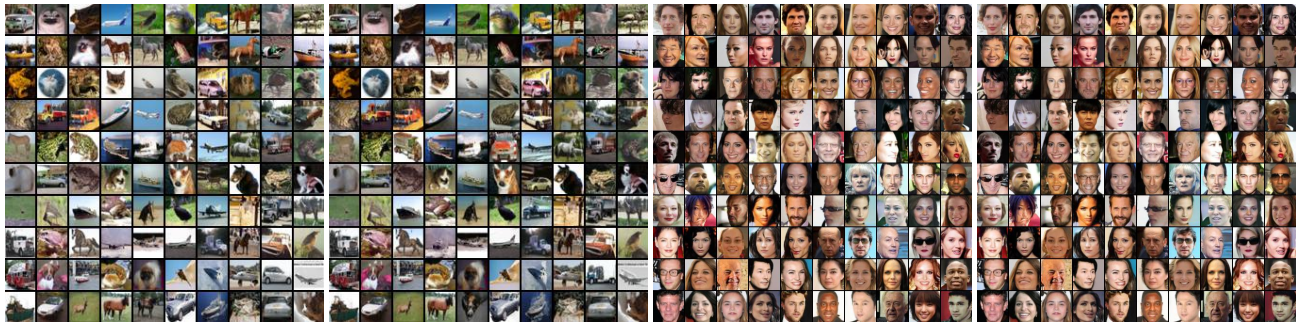
$$\eta_t^* = \begin{cases} \mathbb{E}_{q_t(x_t)} [\mathbf{s}_\theta^t(x_t)], & \text{score prediction;} \\ \mathbb{E}_{q_t(x_t)} [\mathbf{x}_\theta^t(x_t)] - \mathbb{E}_{q_0(x_0)} [x_0], & \text{data prediction;} \\ \mathbb{E}_{q_t(x_t)} [\epsilon_\theta^t(x_t)], & \text{noise prediction;} \\ \mathbb{E}_{q_t(x_t)} [\mathbf{v}_\theta^t(x_t)] + \sigma_t \mathbb{E}_{q_0(x_0)} [x_0], & \text{velocity prediction.} \end{cases} \quad (32)$$

Taking η_t^* into $\mathcal{J}_{\text{DSM}}^t(\theta, \eta_t)$ we can obtain the gap

$$\mathcal{J}_{\text{DSM}}^t(\theta) - \mathcal{J}_{\text{DSM}}^t(\theta, \eta_t^*) = \begin{cases} \frac{1}{2} \left\| \mathbb{E}_{q_t(x_t)} [\mathbf{s}_\theta^t(x_t)] \right\|_2^2, & \text{score prediction;} \\ \frac{\alpha_t^2}{2\sigma_t^2} \left\| \mathbb{E}_{q_t(x_t)} [\mathbf{x}_\theta^t(x_t)] - \mathbb{E}_{q_0(x_0)} [x_0] \right\|_2^2, & \text{data prediction;} \\ \frac{1}{2\sigma_t^2} \left\| \mathbb{E}_{q_t(x_t)} [\epsilon_\theta^t(x_t)] \right\|_2^2, & \text{noise prediction;} \\ \frac{\alpha_t^2}{2\sigma_t^2} \left\| \mathbb{E}_{q_t(x_t)} [\mathbf{v}_\theta^t(x_t)] + \sigma_t \mathbb{E}_{q_0(x_0)} [x_0] \right\|_2^2, & \text{velocity prediction.} \end{cases} \quad (33)$$

C. Visualization of the Generations

We further show generated images in Figure 4 to double confirm the efficacy of our calibration method. We see that model calibration is likely to help to reduce ambiguous generations on both CIFAR-10 and CelebA.



(a) CIFAR-10, w/ model calibration (b) CIFAR-10, w/o model calibration (c) CelebA, w/ model calibration (d) CelebA, w/o model calibration

Figure 4. Unconditional generation results on CIFAR-10 and CelebA using models from Ho et al. (2020) and Song et al. (2021a) respectively. The number of sampling steps is set to 20 based on the results presented in Table 1 and 2. No cherry pick is performed.